Check for updates

NANO · MICRO small
www.small-journal.com

Dislocation-Mediated Hydride Precipitation in Zirconium

Si-Mian Liu, Akio Ishii, Shao-Bo Mi, Shigenobu Ogata, Ju Li,* and Wei-Zhong Han**

The formation of hydrides challenges the integrity of zirconium (Zr) fuel cladding in nuclear reactors. The dynamics of hydride precipitation are complex. Especially, the formation of the butterfly or bird-nest configurations of dislocation structures around hydride is rather intriguing. By in-situ transmission electron microscopy experiments and density functional theory simulations, it is discovered that hydride growth is a hybrid displacive-diffusive process, which is regulated by intermittent dislocation emissions. A strong tensile stress field around the hydride tip increases the solubility of hydrogen in Zr matrix, which prevents hydride growth. Punching-out dislocations reduces the tensile stress surrounding the hydride, decreases hydrogen solubility, reboots the hydride precipitation and accelerates the growth of the hydride. The emission of dislocations mediates hydride growth, and finally, the consecutively emitted dislocations evolve into a butterfly or bird-nest configuration around the hydride.

1. Introduction

Controlling the precipitation of second phases is essential for optimizing the properties of metals.[1,2] The kinetics and thermodynamics of precipitation have been attracted abroad attention.[3–5] Zirconium (Zr) and titanium are widely used in the nuclear and aerospace industries. Owing to their strong affinity to hydrogen, precipitation of hydrides is perceived to be easy.[6,7] Stress-induced hydride reorientation, hydride blistering and delayed hydride cracking threaten the service life of these materials.[8–11] Revealing the mechanism for hydride precipitation is instructive for the development of mitigation strategies.

Different from the pure shear controlled martensitic transformation, the growth of the hydride is reckoned as $1/3[01\bar{1}0]$ partial dislocation shear on the basal plane accompanied by hydrogen diffusion.[12–14] At the crack notch, diffusion-controlled hydride growth is affected by stress gradients and temperature.[15,16] While in the interior of a recrystallized grain, the growth of the hydride depends on the diffusion rate and the concentration of the hydrogen, which are related to the microstructures and stress states.[17,18] Although the in-situ X-ray diffraction (XRD) test revealed some aspects of the precipitation and growth processes of hydrides,[19] detailed processes of hydride precipitation at the micro- and nano-scale are unclear. It is frequently observed that hydrides are surrounded by bird-nest or butterfly-like dislocation structures.[20–24] The appearance of these dislocations is connected to the release of strain energy generated by hydride volume expansion.[25–27] Dislocations not only coordinate the elastoplastic deformation, but also serve as hydrogen traps and hydride nucleation sites.[28] The dislocations accumulated at the hydride tip can remain stable even at high temperatures.[29,30] However, it is difficult to identify the role of dislocations, especially at the early stages of hydride nucleation and growth. Phase-field and molecular dynamics simulations reveal the evolution of hydride morphologies and the formation of dislocation loops.[31–34] However, owing to the lack of in-situ observations, the mechanism of hydride precipitation and their relationship with the complex dislocation structures remain elusive.

Herein, we study the nucleation and growth dynamics of γ-hydride using an in-situ transmission electron microscopy (TEM) technique. The growth of needle-shaped hydrides shows a discontinuous behavior, such as hydride growth-dislocation emission-hydride regrowth. The shear and normal stress field around the needle-shaped hydride during precipitation was calculated using density functional theory. Combining with the thermodynamics and kinetics analysis, we proposed that the stress field induced by the hydride prevents its further growth. Dislocation emission releases stress and decreases the chemical potential of hydrogen at the hydride tip, and further promotes hydride precipitation.

2. Results

2.1. Dynamic Hydride Precipitation

High purity Zr (>99.99%, see composition in Table S1, Supporting Information) with an average grain size of 100 μm was used. Disc Zr foils prepared by twin jet electro-polishing

S.-M. Liu, S.-B. Mi, W.-Z. Han
Center for Advancing Materials Performance from the Nanoscale
State Key Laboratory for Mechanical Behavior of Materials
Xi'an Jiaotong University
Xi'an 710049, China
E-mail: wzhanxjtu@mail.xjtu.edu.cn
A. Ishii, S. Ogata
Department of Mechanical Science and Bioengineering
Osaka University
Osaka 560–8531, Japan
E-mail: ogata@me.es.osaka-u.ac.jp
J. Li
Department of Nuclear Science and Engineering and Department of Materials Science and Engineering
Massachusetts Institute of Technology
Cambridge, Massachusetts 02139, USA
E-mail: liju@mit.edu

The ORCID identification number(s) for the author(s) of this article can be found under https://doi.org/10.1002/smll.202105881.

DOI: 10.1002/smll.202105881

 © 2021 Wiley-VCH GmbH

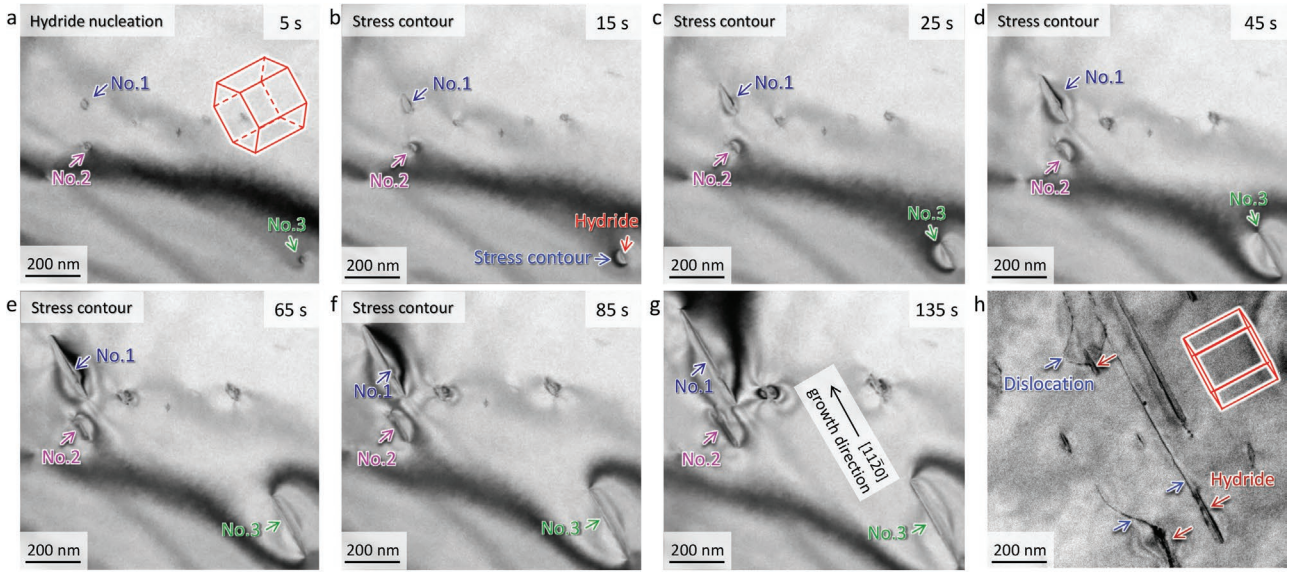

Figure 1. In-situ observation of hydride precipitation. a–g) In-situ video snapshots of the hydride growth at different times; A strong asymmetrical stress field is produced around the hydride during growth; the observation axis is near to [$\bar{2}20\bar{1}$]. See Movie S1, Supporting Information for details. h) Some dislocations were found on the tips and sides of the hydrides after growth. The observation direction is near to [$\bar{1}100$].

were used to study hydride precipitation inside TEM at room temperature. After a few seconds of electron beam exposure, hydrides start to nucleate in the interior of hexagonal close packed (HCP) Zr grains and grow up rapidly, as shown in Movie S1, Supporting Information. A series of bright-field TEM images extracted from the in-situ video are shown in **Figures 1**(a–g). A curved contour with black contrast accompanied the hydride growth, which shows the stress field around a hydride. Under viewing direction of [$\bar{2}20\bar{1}$], no dislocation activity was observed. When turning the zone axis to [$\bar{1}100$], a few dislocations appear at the tips and sides of the hydride, as marked by the blue arrows in Figure 1h. Figure S1a, Supporting Information shows a low magnification bright-field TEM image of this region. All hydrides grow parallel to [11$\bar{2}$0] direction according to the diffraction pattern in Figure S1b, Supporting Information. The hydrides have a lath shape, with thicknesses ranging from 10 to 34 nm (Figure S1c,d, Supporting Information).

Zr thin foil absorbs hydrogen during electro-polishing, and hydride forms under the electron beam irradiation inside TEM. This provides us a chance to monitor the hydride nucleation and precipitation. A few larger hydrides formed during electropolishing because of excessive hydrogen up-taking, as shown in Figure S1e, Supporting Information. A strong stress contour was also observed at the tip of the hydride, and a complex dislocation network wrapped around the hydrides.

Figure 2 shows the real-time observation (at room temperature) of dislocation emissions from tips of a hydride

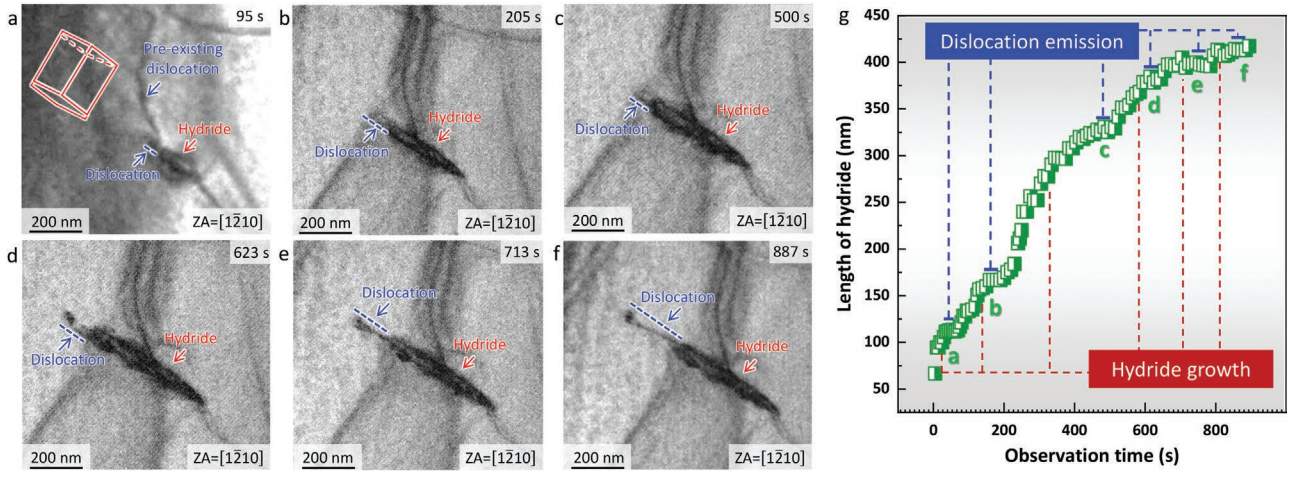

Figure 2. Dislocation emission mediated hydride growth. a,d) Dislocation emission from the hydride tip during the hydride growth at room temperature; e,f) Dislocation reactions occur in the front of hydride tip; g) The length of hydride along the long axis as a function of the time with view direction along [1$\bar{2}$10] zone axis; A hydride growth-dislocation emission-hydride growth sequence is captured. The letters in (g) correspond to the figures (a) to (f). See Movies S2 and S3, Supporting Information for details.

© 2021 Wiley-VCH GmbH

16136829, 2022, 9, Downloaded from https://onlinelibrary.wiley.com/doi/10.1002/smll.202105881 by Massachusetts Institute of Technolo, Wiley Online Library on [26/04/2025]. See the Terms and Conditions (https://onlinelibrary.wiley.com/terms-and-conditions) on Wiley Online Library for rules of use; OA articles are governed by the applicable Creative Commons License

with a viewing direction of [$1\bar{2}10$], which is nucleated on a pre-existing dislocation (see Movies S2 and S3, Supporting Information for details). Without an extra source of hydrogen, the hydride displays a dislocation emission-hydride precipitation-dislocation remission-hydride regrowth sequence. At the recording time of 95 s, the hydride first emits a dislocation at the front tip along its growth direction (Figure 2a). Following that, the hydride grows gradually along the track of the emitted dislocation. After growth for 156 nm, the hydride precipitation rate gradually decreases and finally stops. After dislocation emission from the front of the hydride tip again (Figure 2b), the hydride precipitation reboots. Figures 2c–f record the dislocation emission processes before the hydride regrowth. The two emitted dislocations react with each other in the front of the hydride tip, as shown in Figure 2e,f. The product of the dislocation reaction continues to slip forward; see Movie S3, Supporting Information for more details. The length of the hydride versus the observation time is plotted in Figure 2g. Since the observation direction is along [$1\bar{2}10$], the measured length of hydrides in Figures 2a-f needs to be corrected (by dividing $\cos(\pi/6)$). According to Figure 2g, the dislocation emission occurs immediately at the point of the hydride stopping growth, and once dislocation is reemitted, the hydride regrows in a parabolic kinetics manner (see below). The emission of dislocation is a precursor for hydride precipitation. This is rather similar to the process of lithiation of SnO_2 crystal in lithium-ion batteries, where a diffusive phase transformation is preceded by a tangle of dislocations driving displacive plasticity.[35]

A similar dislocation guided hydride growth characteristic is also captured under the viewing direction of [0001], as shown in **Figure 3** and Movie S4, Supporting Information. Figure 3a–c shows the snapshot of the morphologies of hydride and dislocations during precipitation. The emitted dislocation slips along the *a*-direction according to the image contrast difference (c–a), where D1 represents the position of the emitted dislocation in Figure 3a, and D1' represents the position of the launched dislocation in Figure 3c. The dislocation trace shows that the emitted dislocation at the tip of the hydride glides along the prismatic slip plane, consistent with previous reports.[21,22] After the hydride stops growth, we tune the zone axis to a two-beam condition with $\vec{g} = 11\bar{2}0$, as shown in Figure 3d. Before further growth of the hydride, two dislocations (D1 and D2) are launched, which slip along [$1\bar{2}10$] direction on the ($10\bar{1}0$) plane. Figure 3e illustrates the geometric relationship between the hydride and the emitted dislocation under [0001] observation direction.

During the hydride growth, an emitted dislocation was observed to interact with the inherent <*a*> dislocation in the matrix under [$1\bar{2}10$] zone axis, as shown in **Figure 4** and Movie S5, Supporting Information. First, two dislocations (D1, D2) have been emitted in sequence from the tip of the hydride in the left of Figure 4a. The left hydride nucleates and grows on a preexisting <*a*> dislocation line in the matrix. At t = 54 s, another dislocation (D3) is emitted at the opposite side of the left hydride, which touches the <*a*> dislocation line in the matrix, as indicated by the arrows in Figures 4a-c. Following that, the <*a*> dislocation line bows out (Figure 4b) until it touches the surface of the sample and disappears at t = 107 s (Figure 4c). At the same time, D4 is launched out from the left tip of the left hydride, and D2 continues to slip forward until it encounters D1 (Figure 4d). Finally, D1, D2, and D4 stop in front of the hydride at t = 503 s (Figure 4f). Dislocation emission occurs at both tips of the hydride, not just on one side. As shown in the Movie S5, Supporting Information, the inherent <*a*> dislocation bypasses the right hydride rather than cutting through it. The morphologies of hydrides and dislocations (D1–D4) with different axes and diffraction vectors are shown in Figure 4g–i. Although D1, D2 and D4 show a similar slip behavior in Figure 4a–f, they slip on different prismatic planes, as shown in Figure 4i. The slip direction of D1 and D2 is at an angle of 60° with respect to the growth direction of hydride, while the slip direction of D4 is parallel to the growth direction of hydride, as illustrated in Figure 4j,k. All these in situ videos demonstrate that the emitting of dislocations is a precursor for the hydride precipitation in Zr.

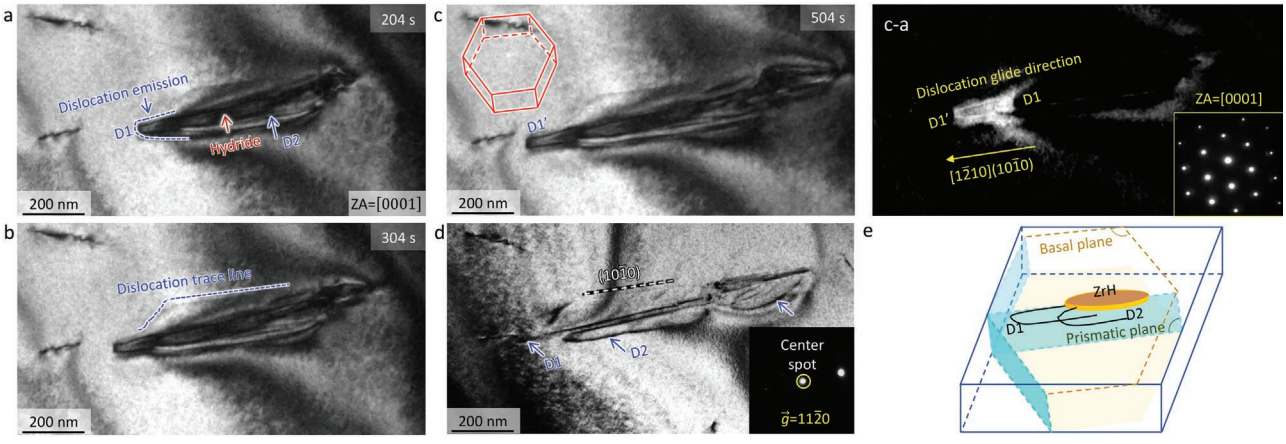

Figure 3. In situ observation of hydride growth viewed along [0001] zone axis. a–c) Snapshots of hydride growth and dislocation emission at different times; (c-a) Image contrast difference between (c) and (a) determine the slip system of the emitting dislocation, i.e., [$1\bar{2}10$]($10\bar{1}0$); d) Dislocation structures produced around the hydride with $\vec{g} = 11\bar{2}0$; e) Illustration of the crystallographic relationship of the hydride precipitation and the dislocation punched out. See Movie S4, Supporting Information for details.

© 2021 Wiley-VCH GmbH

16136829, 2022, 9, Downloaded from https://onlinelibrary.wiley.com/doi/10.1002/smll.202105881 by Massachusetts Institute of Technolo, Wiley Online Library on [26/04/2025]. See the Terms and Conditions (https://onlinelibrary.wiley.com/terms-and-conditions) on Wiley Online Library for rules of use; OA articles are governed by the applicable Creative Commons License

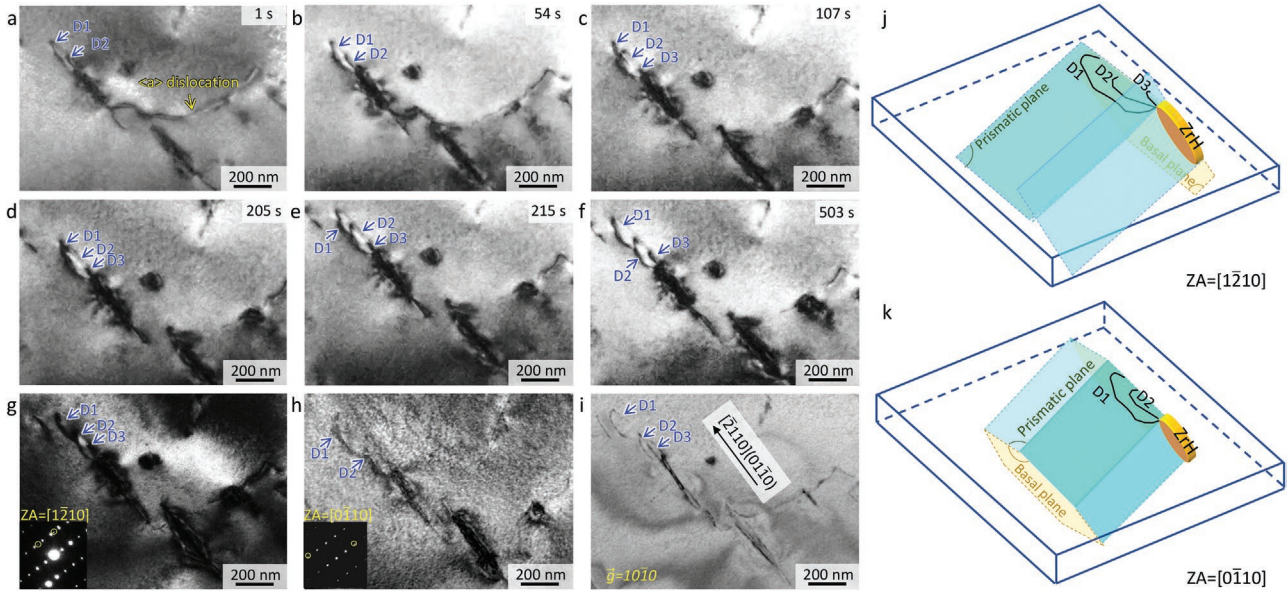

Figure 4. Punching out of series dislocations during hydride growth. a–f) Snapshots of dislocation emission and their interactions in the front of hydride tip at a different time near [1$\bar{2}$10] zone axis; g,h) The TEM images of dislocation after emission under the [1$\bar{2}$10] and [0$\bar{1}$10] zone axis; The yellow circle in the inserts in (g) and (h) indicate the selected area electron diffraction pattern of γ-hydride; i) Dislocation structures produced around the hydride with $\vec{g}=10\bar{1}0$; j,k) Illustration of crystallographic geometry of hydride growth and the punch-out of dislocations under the [1$\bar{2}$10] and [0$\bar{1}$10] zone axis respectively. See Movie S5, Supporting Information for details.

2.2. Stress Around Hydride Tip

A nano-hydride precipitated under in situ TEM observation was characterized by a spherical aberration-corrected electron microscope along $[1\bar{2}10]_{Zr}$ direction. The hydride, with a thickness of 20 nm and a length of approximately 140 nm, is determined as γ-phase with a face-centered tetragonal (FCT) crystal structure according to the diffraction in **Figure 5**a. The orientation relationship between hydride and Zr matrix is $(111)_{\gamma\text{-ZrH}}$// $(0001)_{\alpha\text{-Zr}}$ and $[110]_{\gamma\text{-ZrH}}$// $[1\bar{2}10]_{\alpha\text{-Zr}}$.[13,36] A number of terrace and riser facets are formed at the hydride tip (Figure 5b), which are avenues for emitting dislocations. These steps correspond to the Shockley partial dislocation with the Burgers vector of 1/3[10$\bar{1}$0], as labeled in Figure 5c. The dislocations observed are perfect dislocation with Burgers vector of 1/3<11$\bar{2}$0>,[20–23] which means a dislocation reaction occurs at the interface during precipitation.

Micromechanics analysis using Eigen strain (ε_{xx} = 0.049, ε_{yy} = 0.173, ε_{zz} = 0.006, ε_{xy} = 0.243, ε_{yz} = ε_{xz} = 0) and elastic constants determined by density functional theory (DFT) is used to compute the stress fields around the needle γ-hydride in Figure 5d (see more details in the Supporting Information). Figure S2, Supporting Information plotted the six stress components (σ_{xx}, σ_{yy}, σ_{zz}, τ_{xy}, τ_{yz}, τ_{xz}) around the hydride tip after transformation. The shear stress τ_{xy} is much larger than the normal stress (σ_{xx}, σ_{yy}, σ_{zz}) and the effects of τ_{yz} and τ_{xz} are negligible. Figure 5f shows the von-Mises stress condition around the hydride tip. The normal stress components and the shear stress cancel out. The computed shear stress component is projected onto the specific slip systems in order to compare the level of produced shear stress with the critical resolved shear stress (CRSS) on that slip system, as shown in Figure 5g–i and Figure S3, Supporting Information. During precipitation, compressive and shear back stresses accumulated inside the hydride, as shown by the blue color in Figure S2, Supporting Information. A strong tensile and shear stress fields accumulated in the front of the hydride in HCP Zr. The stress projected on three prismatic planes (Figure 5g–i) is all larger than the CRSS of the prismatic slip system (τ_{pris} = 2.0 GPa), hence dislocations on the prismatic slip system are easy to glide and carry out displacive plasticity. This is consistent with our observation of dislocation emitting on different prismatic planes (Figure 4). The projections of the stress on both the basal and pyramidal planes are shown in Figure S3, Supporting Information. The magnitude of the stress projection is higher than the CRSS of the basal (τ_b = 2.6 GPa (DFT)) and the pyramidal (τ_p = 2.4 GPa (DFT)) slip systems as well. Therefore, all possible slip systems in Zr can be activated after the hydride precipitation, providing the possibility of producing a butterfly or bird-nest dislocation configuration. We only observed the activation of prismatic slip systems in this experiment because of the thin foil sample geometry (Figures 2–4). The above CRSS were all computed by using DFT-based ideal shear strength analysis.[37,38] The ideal shear stress can be reached at the tip of γ-hydride owing to the large volumetric transformation strain of 17.7%, hence dislocations easily nucleate at the hydride tip, and subsequently glide quite far away. This in turn relaxes the near-tip hydrostatic tensile stress, making the hydrogen supersaturated in the Zr matrix, and assisting the heterogeneous hydride growth along the dislocation cores. The actual CRSS necessary to nucleate the dislocation should be lower than the ideal shear stress because of the interfacial dislocations,[39,40] atomic-scale steps at the interface, and finite temperature effect.[41] Therefore, the above ideal shear stress is the sufficient condition for the dislocation nucleation, but not the necessary requirement.

© 2021 Wiley-VCH GmbH

16136829, 2022, 9, Downloaded from https://onlinelibrary.wiley.com/doi/10.1002/smll.202105881 by Massachusetts Institute of Technolo, Wiley Online Library on [26/04/2025]. See the Terms and Conditions (https://onlinelibrary.wiley.com/terms-and-conditions) on Wiley Online Library for rules of use; OA articles are governed by the applicable Creative Commons License

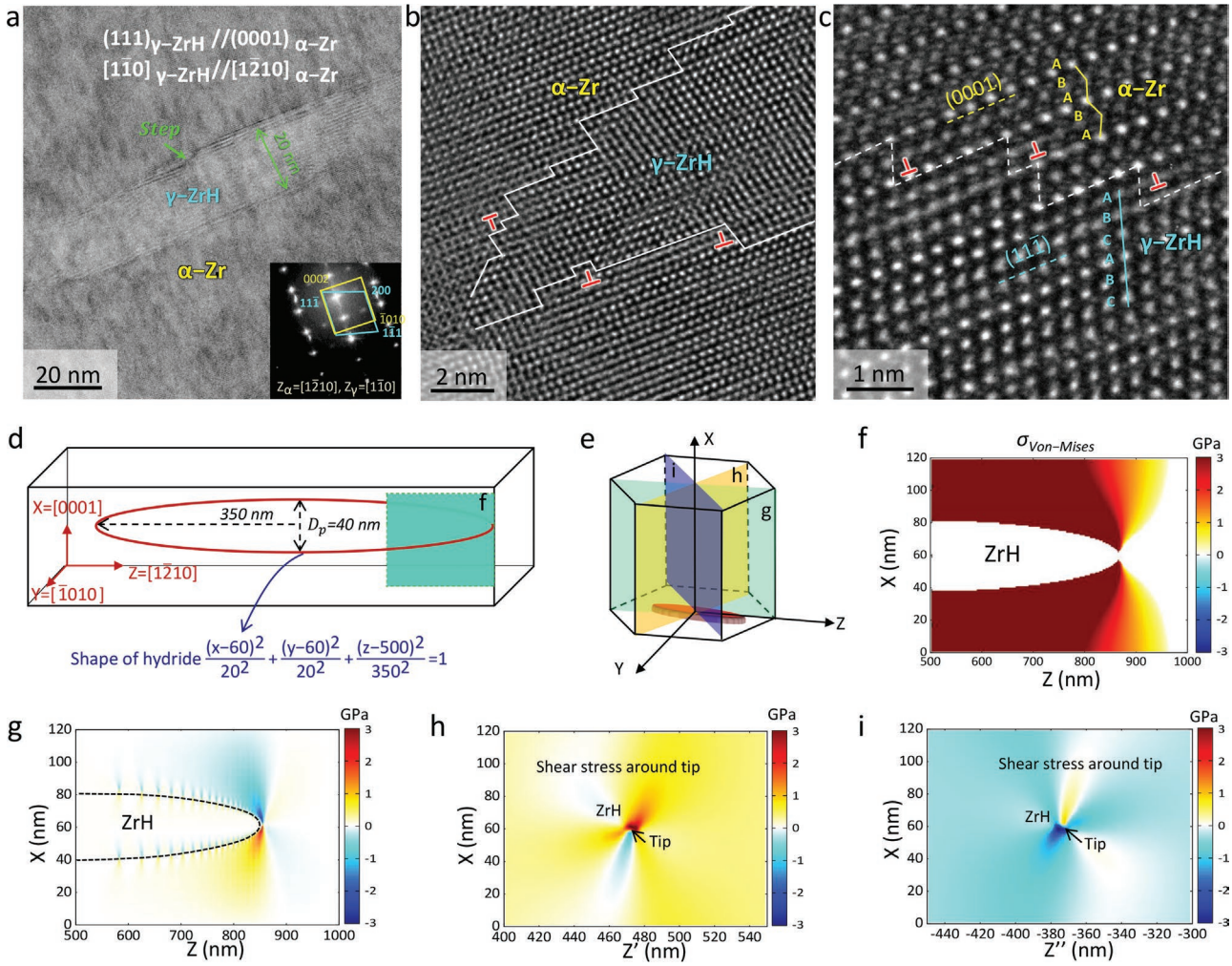

Figure 5. Atomic structure and stress field around the hydride tip. a–c) Atomic-scale images of interface between γ-hydride and α-Zr. (a) Steps are identified at the interface; (b) high-resolution TEM image of the hydride tip; (c) dislocations at the interface of γ-hydride and α-Zr. d–i) stress field around the hydride. (d) The shape model of a needle-liked hydride. (e) Schematic diagram of hydride and prismatic slip system of punched-out dislocations in Zr. (f) The von-Mises stress around a hydride tip. The normal stress and the shear stress inside the hydride cancel out. g–i) The projection of the shear stress component τ_{yz} around hydride tip on the three prismatic slip systems:(g) [1$\bar{2}$10] ($\bar{1}$010); (h) [$\bar{2}$110] (01$\bar{1}$0); (i) [11$\bar{2}$0] ($\bar{1}$100).

3. Discussion

3.1. Effect of Electron-Beam on Hydride Precipitation

The solubility of hydrogen in HCP Zr is extremely low at room temperature, less than 20 ppm.[7] When hydrogen concentration is extremely low, in general, the nucleation of hydride is more difficult because it requires the spontaneous aggregation of hydrogen atoms from a very large surrounding region to achieve strong solute partitioning. Therefore, the electron beam plays a key role in the nucleation of the hydride. The beam with 200 keV energy is too weak to knock a Zr atom out, but easily knocks out oxygen atoms from the oxide layer and creates a number of O vacancies.[42] These knock-outs can also happen at the ZrO_2-Zr interface region, where there is a range of Zr valence states,[43] and it is conceivable that O vacancies in the interfacial region can be converted into Zr vacancy in the adjacent HCP crystal, resulting in the inward diffusion of Zr vacancies from surface to the subsurface of the sample. The hydrogen absorbed during electron-polishing is mainly as interstitials in thin foil Zr. The binding energy of a vacancy with an oxygen atom is 1 kJ mol^{-1} while with a hydrogen atom is $-22 \approx -17$ kJ mol^{-1}, which means the vacancies in HCP Zr assist the accumulation of hydrogens via trapping.[44–46] The binding energy of a vacancy with four hydrogen atoms is -87 kJ mol^{-1},[45] which means once hydrogens are captured by vacancy, they prefer to form a stable hydrogen-vacancy complex in HCP Zr. Furthermore, the vacancy carrying hydrogens can even move faster and is therefore easier to gather together.[47] This facilitates the nucleation of hydride embryos, which requires a large number of highly concentrated hydrogen. Figure S4, Supporting Information, shows one example of a nano hydride nucleation at the subsurface of the sample and inward growth into the Zr matrix (see Movie S6, Supporting Information). An oxide layer with a thickness of 16 nm is covering the Zr thin foil. After exposure to an electron beam for 147 s, the hydride

© 2021 Wiley-VCH GmbH

16136829, 2022, 9, Downloaded from https://onlinelibrary.wiley.com/doi/10.1002/smll.202105881 by Massachusetts Institute of Technolo, Wiley Online Library on [26/04/2025]. See the Terms and Conditions (https://onlinelibrary.wiley.com/terms-and-conditions) on Wiley Online Library for rules of use; OA articles are governed by the applicable Creative Commons License

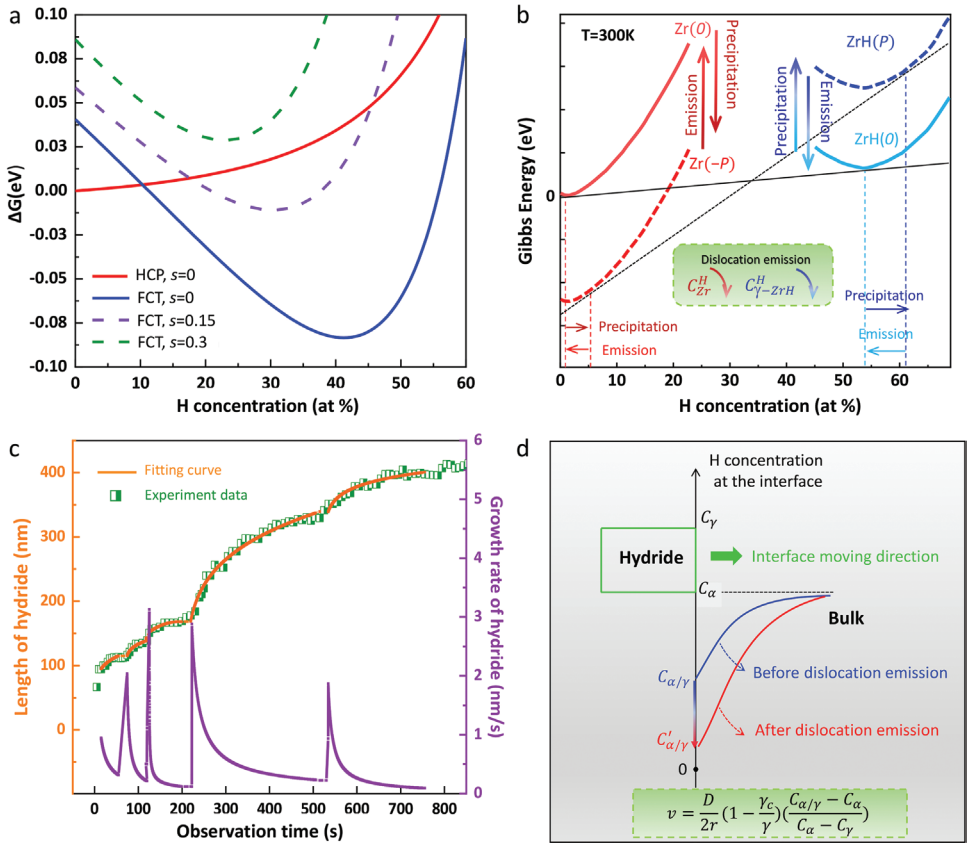

Figure 6. Gibbs free energy curves of hydride precipitation and growth law. a) The variations of Gibbs free energy per Zr atom ΔG with respect to hydrogen concentration and stress for α-Zr (HCP) and FCT structures. s represents the degree of transformation strain along the transformation path (see Supporting Information 3). b) The effect of dislocation emission dislocations on the Gibbs free energy curve in hydride precipitation. The red curve is the Gibbs free energy curve of α-Zr.[15] When the hydride growth, the Gibbs free energy curve decreases (from solid to dash line) due to the accumulation of normal (tensile) and shear stresses in α-Zr at the front of hydride, which increases the solubility of hydrogen in α-Zr. The dislocation emission releases the stress concentration, which reduces the solubility of hydrogen in Zr in front of hydride, thus promoting the migration of the hydride-α-Zr interface. c) The variation of the length of hydride in Figure 2g with time and its growth rate curve (purple lines). The fitting curve follows the parabola law of diffusion-controlled growth. d) The hydrogen concentration and its gradient at interface before and after dislocation emission.

embryo started to form at the interface and then grow inward (Figure S4b, Supporting Information). Therefore, the electron beam irradiation-induced vacancies assist hydride nucleation.

3.2. Dislocation Emission and Hydrogen Solubility

The growth of hydrides requires a continuous supply of hydrogen and a concentration gradient near the interface. It is well known that the distribution of hydrogen can be affected by stress.[32–34] The variation of Gibbs free energy for one Zr atom with hydrogen concentration and stress for HCP (α-Zr with H) and FCT (hydride) structures were computed (see more details inthe Supporting Information) and plotted in **Figure 6**a. The solution of the elasticity problem leads to stresses between 2 and 5 GPa at the hydride/Zr interface. Therefore, dislocation emission happens to relieve the shear and normal stresses.

Figure 6b analyzes the variation of Gibbs free energy curves before and after the release of dislocations assuming that the dislocations fully release the stress field at the hydride tip. The red and blue solid lines represent the stress-free state of the Gibbs free energy curve of Zr and γ-hydride, respectively. Because the precipitation of the hydride causes the matrix to bear the tensile and shear stresses, and the compressive and shear back stresses inside the hydride (Figure S2, Supporting Information), the Gibbs free energy of the matrix decreases and the Gibbs free energy of the hydride increases, as shown by the red and blue dotted lines in Figure 6c. Hence, the equilibrium condition of hydride precipitation is altered, which decreases the chemical potential and increases the hydrogen solubility of the Zr matrix. Without further hydrogen supply, the increase of hydrogen solubility in Zr and the stress around the hydride tip stop hydride precipitation.

In order to reduce the total free energy, hydrides start to emit dislocations to release the accumulated stress, which reduces the equilibrium hydrogen solubility in HCP Zr in front of the hydride tip, then the hydride restart to grow. This is the origin of the regrowth of hydride and the release of dislocations alternately in experiments (Figures 2 and 3). When the hydrogen source is depleted, even if the dislocations are released, there is no further hydride precipitation. A similar phenomenon of precipitate growth catalyzed by dislocations has also been observed in steel.[48]

© 2021 Wiley-VCH GmbH

16136829, 2022, 9, Downloaded from https://onlinelibrary.wiley.com/doi/10.1002/smll.202105881 by Massachusetts Institute of Technolo, Wiley Online Library on [26/04/2025]. See the Terms and Conditions (https://onlinelibrary.wiley.com/terms-and-conditions) on Wiley Online Library for rules of use; OA articles are governed by the applicable Creative Commons License

The dislocation emission also controls the kinetic process of hydride growth. The length of the hydrides versus the observation time in Figure 2g follows a parabola growth law, although each growth stage is separated by the dislocation emission. We plotted the fitted curve of each segment in Figure 6c again and also plotted its differentiation-the growth rate of hydride. After punching out of dislocations from the tip of the hydride, the growth rate of the hydride shows a sharp increase, then decays gradually (purple line in Figure 6c). According to the normal diffusion-controlled plate-shaped phase growth, the moving rate (v) of the hydride front can be described by the Zener-Hillert equation:[3–5]

$$v = \frac{D_H}{2r}\left(1-\frac{r_c}{r}\right)\left(\frac{C_{\alpha/\gamma}-C_\alpha}{C_\alpha-C_\gamma}\right) \quad (1)$$

where r is the radius of curvature of the hydride tip and r_c is the critical radius, at which the hydride stops growth. D_H is the diffusion coefficient of hydrogen in HCP Zr. $C_{\alpha/\gamma}$ is the hydrogen concentration in HCP Zr at the hydride interface, C_γ is the hydrogen concentration inside the hydride and C_α is the bulk hydrogen concentration in HCP Zr far from the hydride.

During the growth of the needle-shaped hydride (Figures 1–4), the front radius r changes little. The diffusion coefficient D_H, which depends on activation energy and temperature, is assumed to be constant. After the dislocation emission, the sharp increase in the growth rate indicates that the concentration gradient near the hydride interface has a sudden change, as marked in Figure 6d. Assuming C_γ and C_α remain constant, the reduction of the hydrogen concentration near the interface $C_{\alpha/\gamma}$ (see Figure 6d) leads to a high hydride migration rate. This is consistent with the analysis of the Gibbs free energy curves in Figure 6b, as in long-range transport dominated kinetics, interfacial reaction (hydrogen exchange between α and γ phases) is assumed to be facile and so $C_{\alpha/\gamma}$ should be close to the thermodynamic equilibrium after the Gibbs-Thomson effect has been taken into account (the $1-\frac{r_c}{r}$ factor), and therefore the actual $C_{\alpha/\gamma}$ is controlled facilely by the disparate stresses in the two adjacent phases. Therefore, dislocation emission from the hydride tip mediates hydride growth and also tunes the growth rate of the hydrides under current experimental conditions of relatively low hydrogen concentration and at room temperature.

4. Conclusion

The precipitation of γ-hydride shows a dislocation emission-hydride precipitation-dislocation remission-hydride regrowth sequence, which is a strongly coupled displacive-diffusive process. Hydride precipitation builds up large shear stress and tensile stress around the hydride tip in Zr matrix, which increases the solubility of hydrogen and prevents hydride growth. Dislocation emission reduces the hydrostatic tensile and shear stress, decreases the hydrogen solubility and reboots the hydride precipitation. It also decreases the hydrogen concentration at the interface at the HCP Zr side, increases the concentration gradient and leads to a marked increase in growth rate. Finally, the emitted dislocations produce a complex dislocation network that wraps around the hydride in a butterfly or bird-nest-like tangle.

5. Experimental Section

Sample Preparation: High-purity Zr (>99.99 wt.%) with low levels of trace elements (Table S1, Supporting Information) was used in this experiment. The sample was annealed in an argon atmosphere for 72 h at 800 °C in order to obtain homogeneous microstructures with a large grain size (>100 µm) and a low dislocation density. The TEM sample was prepared by mechanically ground to a thickness of 50 µm and subsequently electro-polished using a solution of 10% perchloric acid in ethanol at −30 °C. After electronic polishing, the sample was used for in-situ observation immediately.

In-Situ Observation in TEM: The characterization and in-situ observation experiments were carried out with a double tilting holder inside a JEOL 2100F at room temperature. The sample was irradiated by the 200 keV electron beam during characterization. The observation used a beam density of 20 pA cm^{-2}. Real-time observation was recorded by a charge-coupled device camera (ORIUS 833 SC200D, Gatan Inc., Pleasanton, CA) at 10 frames per second. The FEI Titan 80–300 microscope (operated at 300 kV) with an aberration corrector for the objective lens was used to characterize the atomic-resolution interface structure of hydride/α-Zr.

Stress Field Simulations: Based on atomic structure optimization analysis using VASP code,[49,50] the Eigen strain $\varepsilon^{(FCT\text{-}ZrH)}$ generated by the Zr-ZrH transformation (transformation strain) was computed by density functional theory (DFT). Once transformation strain $\varepsilon^{(FCT\text{-}ZrH)}$ is calculated, the internal stress field around the FCT γ-hydride needle precipitation in Zr can be estimated using a micromechanics approach.[51] More details of DFT computation and micromechanics analysis of stress field are shown in Supporting Information. A model with a dimension of 120 nm × 120 nm × 1000 nm Zr matrix having a 40 nm × 40 nm × 700 nm ellipsoidal needle-liked ZrH inclusion was constructed for simulation (Figure 5d).

Critical Shear Stress Computations: Using the VASP DFT code,[49,50] the critical shear stress was computed by applying pure shear deformation on the primitive cell of α-Zr along its slip system.[37,38] 13 × 13 × 13 k-point mesh is used. The other DFT computational conditions are the same as in the stress field simulations.

Supporting Information

Supporting Information is available from the Wiley Online Library or from the author.

Acknowledgements

The author thank Prof. Christopher Hutchinson (Monash University) and Prof. Irene Beyerlein (UCSB) for fruitful discussion. This work was supported by the National Natural Science Foundation of China (Grant Nos. 51922082, 51971170 and 51942104), the National Key Research and Development Program of China (2017YFB0702301), the 111 Project of China (Grant Number BP2018008) and the Innovation Project of Shaanxi Province (grant number 2017KTPT-12). S.O. acknowledges the support by JSPS KAKENHI Grant No. JP17H01238 and Element Strategy Initiative for Structural Materials (ESISM) of MEXT, Grant No. JPMXP0112101000.

Conflict of Interest

The authors declare no conflict of interest.

© 2021 Wiley-VCH GmbH

16136829, 2022, 9, Downloaded from https://onlinelibrary.wiley.com/doi/10.1002/smll.202105881 by Massachusetts Institute of Technolo, Wiley Online Library on [26/04/2025]. See the Terms and Conditions (https://onlinelibrary.wiley.com/terms-and-conditions) on Wiley Online Library for rules of use; OA articles are governed by the applicable Creative Commons License

Author Contributions

S.-M.L., A.I., contributed equally to this work. W.Z.H. designed the project. S.M.L. conducted the in-situ experiments under the guidance of W.Z.H. A.I. and S.O. performed the density functional theory (DFT) and the micromechanics calculations. S.B.M performed the high-resolution transmission electron microscopy observation. S.M.L., S.O., J.L. and W.Z.H. wrote the manuscript. All authors discussed and analyzed the results and contributed to the theoretical analysis.

Data Availability Statement

The data that support the findings of this study are available from the corresponding author upon reasonable request.

Keywords

dislocation, hydrides, precipitation, stress, zirconium

Received: September 25, 2021
Revised: November 28, 2021
Published online: December 18, 2021

[1] J. da Costa Teixeira, D. G. Cram, L. Bourgeois, T. J. Bastow, A. J. Hill, C. R. Hutchinson, *Acta Mater.* **2008**, *56*, 6109.
[2] Y. Chen, X. Y. Fang, Y. Brechet, C. R. Hutchinson, *Acta Mater.* **2014**, *81*, 291.
[3] J. Bloch, M. H. Mintz, *J. Alloys Compd.* **1997**, *253*, 529.
[4] M. Hillert, L. Höglund, J. Agren, *Acta Mater.* **2003**, *51*, 2089.
[5] J. Agren, Y. Brechet, C. R. Hutchinson, J. M. Philibert, *Thermodynamics and Phase Transformations, de Physique*, EDP Sciences, France **2008**.
[6] C. Q. Chen, S. X. Li, K. Lu, *Acta Mater.* **2003**, *51*, 931.
[7] A. T. Motta, L. Capolungo, L. Q. Chen, M. N. Cinbiz, M. R. Daymond, D. A. Koss, E. Lacroix, G. Pastore, P. A. Simon, M. R. Tonks, B. D. Wirth, M. A. Zikry, *J. Nucl. Mater.* **2019**, *518*, 440.
[8] J. Song, W. A. Curtin, *Acta Mater.* **2011**, *59*, 1557.
[9] P. Vizcaíno, J. R. Santisteban, M. A. Vicente Alvarez, A. D. Banchik, J. Almer, *J. Nucl. Mater.* **2014**, *447*, 82.
[10] R. L. Eadie, C. E. Coleman, *Scr. Metall.* **1989**, *23*, 1865.
[11] F. Long, D. Kerr, G. Domizzi, Q. Wang, M. .R. Daymond, *Acta Mater.* **2017**, *129*, 450.
[12] Y. F. Zhang, X. M. Bai, J. Yu, M. R. Tonks, M. J. Noordhoek, S. R. Phillpot, *Acta Mater.* **2016**, *111*, 357.
[13] G. J. C. Carpenter, *Acta Metall.* **1978**, *26*, 1225.
[14] S. Banerjee, P. Mukhopadhyay, *Phase Transformations – Examples from Titanium and Zirconium Alloys, Pergamon materials series, Pergamon*, Elsevier Science, Burlington **2007**.
[15] X. Q. Ma, S. Q. Shi, C. H. Woo, L. Q. Chen, *Comput. Mater. Sci.* **2002**, *23*, 283.
[16] Q. Shi, *J. Nucl. Mater.* **1999**, *275*, 318.
[17] M. Hillert, *Acta Metall.* **1999**, *47*, 4481.
[18] M. Puls, *J. Nucl. Mater.* **2009**, *393*, 350.
[19] K. B. Colas, A. T. Motta, J. D. Almer, M. R. Daymond, M. Kerr, A. D. Banchik, P. Vizcaino, J. R. Santisteban, *Acta Mater.* **2010**, *58*, 6575.
[20] J. E. Bailey, *Acta Metall.* **1963**, *11*, 267.
[21] J. S. Bradbrook, G. W. Lorimer, N. Ridley, *J. Nucl. Mater.* **1972**, *42*, 142.
[22] G. J. C. Carpenter, *J. Nucl. Mater.* **1973**, *48*, 267.
[23] G. C. Weatherly, *Acta Metall.* **1981**, *29*, 501.
[24] D. O. Northwood, D. T. H. Lim, *Metallography* **1981**, *14*, 21.
[25] G. J. C. Carpenter, *J. Nucl. Mater.* **1973**, *48*, 264.
[26] S. Shibata, M. Taya, T. Mori, T. Mura, *Acta Metall. Mater.* **1992**, *40*, 3141.
[27] G. P. M. Leyson, B. Grabowski, J. R. Neugebauer, *Acta Mater.* **2015**, *89*, 50.
[28] V. Perovic, G. C. Weatherly, C. J. Simpson, *Scr. Metall.* **1982**, *16*, 409.
[29] G. J. C. Carpenter, *J. Nucl. Mater.* **1978**, *73*, 190.
[30] Y. Shinohara, H. Abe, T. Iwai, N. Sekimura, T. Kido, H. Yamamoto, T. Taguchi, *J. Nucl. Sci. Technol.* **2009**, *46*, 564.
[31] X. H. Guo, S. Q. Shi, Q. M. Zhang, X. Q. Ma, *J. Nucl. Mater.* **2008**, *378*, 120.
[32] X. Q. Ma, S. Q. Shi, C. H. Woo, L. Q. Chen, *Mech. Mater.* **2006**, *38*, 3.
[33] H. Tummala, L. Capolungo, C. N. Tome, *J. Nucl. Mater.* **2018**, *511*, 406.
[34] T. W. Heo, K. B. Colas, A. T. Motta, L. Chen, *Acta Mater.* **2019**, *181*, 262.
[35] J. Y. Huang, L. Zhong, C. M. Wang, J. P. Sullivan, W. Xu, L. Q. Zhang, S. X. Mao, N. S. Hudak, X. H. Liu, A. Subramanian, H. Fan, L. Qi, A. Kushima, J. Li, *Science* **2010**, *330*, 1515.
[36] Y. J. Jia, I. J. Beyerlein, W. Z. Han, *Acta Mater.* **2021**, *216*, 117146.
[37] S. Ogata, J. Li, S. Yip, *Science* **2002**, *298*, 807.
[38] S. Ogata, J. Li, N. Hirosaki, Y. Shibutani, S. Yip, *Phys. Rev. B* **2004**, *70*, 104104.
[39] F. Z. Dai, Z. P. Sun, W. Z. Zhang, *Acta Mater.* **2020**, *186*, 124.
[40] P. A. Geslin, R. Gatti, B. Devincre, D. Rodney, *J. Mech. Phys. Solids* **2017**, *108*, 49.
[41] Du, J. P. , Wang, Y. J. , Lo, Y. C. , Wan, L. , Ogata, S. , *Phys. Rev. B* **2016**, *95*, 104114.
[42] J. A. Sundararajan, M. Kaur, Y. Qiang, *J. Phys. Chem. C* **2015**, *119*, 8357.
[43] Y. Dong, A. T. Motta, E. A. Marquis, *J. Nucl. Mater.* **2013**, *422*, 270.
[44] M. Christensen, W. Wolf, C. Freeman, E. Wimmer, R. B. Adamson, L. Hallstadius, P. E. Cantonwine, E. V. Mader, *J. Phys.: Condens. Matter* **2015**, *27*, 025402.
[45] C. I. Maxwell, E. Torres, J. Pencer, *J. Nucl. Mater.* **2018**, *511*, 341.
[46] M. Christensen, W. Wolf, C. Freeman, E. Wimmer, R. B. Adamson, L. Hallstadius, P. E. Cantonwine, E. V. Mader, *J. Nucl. Mater.* **2014**, *445*, 241.
[47] J. P. Du, W. T. Geng, K. Arakawa, J. Li, S. Ogata, *J. Phys. Chem. Lett.* **2020**, *11*, 7015.
[48] J. Du, F. Mompiou, W. Zhang, *Scr. Mater.* **2018**, *145*, 62.
[49] G. Kresse, J. Furthmuller, *Phys. Rev. B* **1996**, *54*, 11169.
[50] G. Kresse, D. Joubert, *Phys. Rev. B* **1999**, *59*, 1758.
[51] T. Mura, *Micromechanics of Defects in Solid*, Springer Science & Business Media, New York **2013**.

 © 2021 Wiley-VCH GmbH

16136829, 2022, 9, Downloaded from https://onlinelibrary.wiley.com/doi/10.1002/smll.202105881 by Massachusetts Institute of Technolo, Wiley Online Library on [26/04/2025]. See the Terms and Conditions (https://onlinelibrary.wiley.com/terms-and-conditions) on Wiley Online Library for rules of use; OA articles are governed by the applicable Creative Commons License